ACS APPLIED MATERIALS & INTERFACES

Research Article

www.acsami.org

Morphological Effects on the Small-Molecule-Based Solution-Processed Organic Solar Cells

Dong-Chan Lee,*[,†] Lacie V. Brownell,[†] Liang Yan,[‡] and Wei You[‡]

[†]Department of Chemistry, University of Nevada, Las Vegas, 4505 S. Maryland Parkway, Box 454003, Las Vegas, Nevada 89154-4003, United States

[‡]Department of Chemistry, University of North Carolina at Chapel Hill, Chapel Hill, North Carolina 27599-3290, United States

Supporting Information

ABSTRACT: We report a proof-of-concept study on solution-processed organic solar cells (OSCs) based on [6,6]-phenyl-C_{61}-butyric acid methyl ester ($PC_{61}BM$) and structurally compact donor molecules which have dithiophene−phenazine−dithiophene (**TH-P**) and dithiophene−quinoxaline−dithiophene (**TH-Q**) configurations with decyloxy and methyl side groups, respectively. These molecules formed one-dimensional fibers through self-assembly via weak nonbonding interactions such as $\pi-\pi$ and van der Waals interactions even during a fast solvent removal process such as spin-casting. Photophysical and thermal properties of the new donor molecules were characterized with UV−vis absorption and fluorescence spectroscopy, differential scanning calorimetry, and thermogravimetric analysis. The electrochemical data determined experimentally were correlated well with theoretical evaluations. The fibers from the two donor molecules showed distinct morphological differences, allowing for in-depth investigations into their influence on the OSC performance. A continuous three-dimensional network of endless one-dimensional nanofibers, with a width of 300−400 nm, were formed from **TH-P** regardless of the presence of $PC_{61}BM$, affording spontaneous nanoscale phase separation that facilitates a large donor/acceptor interfacial area. Bulk (BHJ) and planar heterojunctions (PHJ) from **TH-P**/$PC_{61}BM$ showed a power conversion efficiency (PCE) of 0.38% and 0.30%, respectively, under optimum device conditions. Post thermal annealing led to the increased domain size and a major decrease in J_{sc}. Meanwhile, shorter, more rigid needles with a large thickness variation were formed from **TH-Q**. A continuous network of **TH-Q** was obtained by spin-coating only in the presence of $PC_{61}BM$, and the PCE of **TH-Q**/$PC_{61}BM$ BHJ was found to be 0.36%. However, the PHJ showed poor device performance due to **TH-Q**'s inability to form a continuous film by spin-coating. The present study suggests a basic molecular architecture to drive one-dimensional assembly and demonstrates the significance of fibrillation for small-molecule-based OSCs.

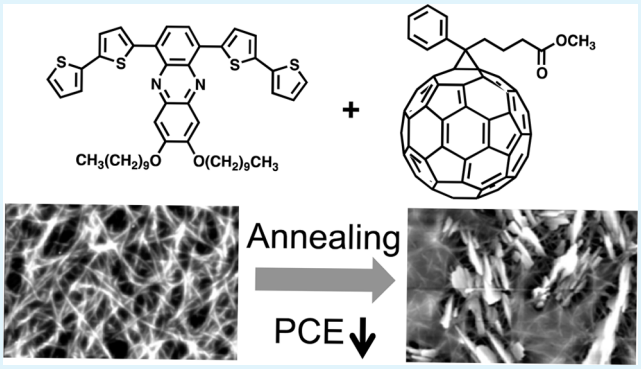

KEYWORDS: *organic solar cell, self-assembly, fibrillation, donor−acceptor−donor, phenazine, quinoxaline*

INTRODUCTION

Solution processability is one of the most prominent advantages of organic solar cells (OSCs) as it allows for low-cost device fabrication without restriction in size and shape for substrates/devices. Bulk heterojunctions (BHJs) of a donor polymer and a fullerene acceptor[1−12] have been the major player for solution-processable OSCs. Macroscopic high-quality films of the donor polymer and the acceptor can be achieved by simple spin-casting in which appropriate phase separations of each component facilitate exciton dissociation and charge carrier transport. Despite impressive advances, the intrinsic molecular weight distribution, that is, nonunity polydispersity index (unless prepared by living polymerizations), could cause issues associated with batch-to-batch consistency and purity. In this regard, small-molecule-based OSCs have been receiving a growing interest as they can provide better control on the electronic property tuning, purification, and device consistency.[13,14] Reports have demonstrated that small molecules have potential to be competitive active materials for solution-processed OSCs,[13−21] reaching power conversion efficiencies (PCE) up to 7−8%[15−19]; however, many of the small-molecule based OSCs are still inferior to their polymeric counterparts. For solution-processed OSCs, high-quality films with appropriate phase separation of donor and acceptor components (especially for BHJ) must be made during fast solvent removal. However, one of the drawbacks of small molecules, especially when the molecular weight is low, is a lack of capability to produce interpenetrating networks due to their tendency to aggregate/crystallize. A promising approach to mitigate the problem is producing one-dimensional (1D) fibers utilizing

Received: May 5, 2014
Accepted: August 28, 2014
Published: August 28, 2014

self-assembly. 1D assembly resembles polymerization; however, it uses nonbonding interactions in one direction rather than covalent bond formation in a typical polymerization. Thus, proper molecular design is critical so that intermolecular interactions in the main growth direction can be preferred, while growth in the other direction(s) should be retarded by other means, for example, interactions with solvent molecules. It should be noted that the recent reports emphasize the positive effects of fibrous morphology on the PCE of organic solar cells.[22−33] In fact, nanoscale phase separation of the donor and acceptor can be achieved spontaneously without the need of controlling process conditions, which also renders post thermal treatment unnecessary. For example, fibrillation can be driven by strong directional interactions such as hydrogen bonding[30,34−36]; however, the requirement of specific functional groups for the interaction could limit design flexibility due to synthetic accessibility of these specific functionalities. For efficient charge transport in organic semiconductors, effective intermolecular π-orbital overlap is crucial. Therefore, it would be ideal to drive the assembly via intermolecular $\pi-\pi$ interactions. Unfortunately, molecular 1D assembling systems for OSCs driven only by weak nonbonding interactions are rare to find, hampering understanding of the required molecular architecture to drive such an assembly.

In this paper, we report two new donor molecules for OSCs with compact molecular design comprising probably the simplest π-core and solubilizing group. Yet they are capable of forming 1D fibers using weak nonbonding interactions via solution processes. The systems allow for fundamental investigations on the effect of fiber network on the device performance. Furthermore, the structural difference of the donor molecules produced fibers with different morphologies, enabling a comparative structure−morphology−performance study.

RESULTS AND DISCUSSIONS

As shown in Figure 1, the donor molecules have bithiophene−phenazine−bithiophene (**TH-P**) and bithiophene−quinoxaline−bithiophene (**TH-Q**) structures. They have configurations of electron-accepting moieties sandwiched by electon-donating thiophenes to take advantage of orbital mixing, resulting in band gap compression. **TH-P** contains decyloxy side groups on the phenazine core, while **TH-Q** has only methyl groups on its quinoxaline core. The difference in the alkyl side groups is expected to affect the morphology of the assembled structures. Detailed synthetic procedures are provided in the Supporting Information (SI). The key synthetic step was the Stille coupling of [2,2′]bithiophenyl-5-yl-tributyl-stannane with 1,4-dibromo-7,8-bis(decyloxy)phenazine (for **TH-P**) and 5,8-dibromo-2,3-dimethylquinoxaline (for **TH-Q**) using $Pd(PPh_3)_4$ as the catalyst. The target compounds were fully characterized by ^1H and ^{13}C NMR spectroscopy, mass spectrometry, and elemental analysis to confirm their structural integrity.

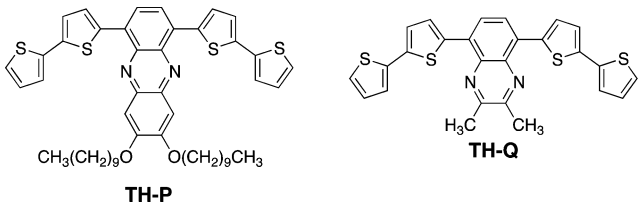

Figure 1. Structures of thiophene-containing phenazine (**TH-P**) and quinoxaline (**TH-Q**).

The absorption maximum (λ_{max}) for **TH-P** was 513 nm, which is longer than that of **TH-Q** (462 nm) in $CHCl_3$ (Figure 2). However, the absorptivity of **TH-P** (2.1×10^4 cm^{-1} M^{-1}) was lower than that of **TH-Q** (3.3×10^4 cm^{-1} M^{-1}) at their respective λ_{max}. In the solid state (cast films from $CHCl_3$ solutions), both compounds showed noticeable red shifts in their absorptions, indicating the presence of intermolecular $\pi-\pi$ interactions.[37] The extent of red shift was higher for **TH-Q**, suggesting more significant $\pi-\pi$ interactions.

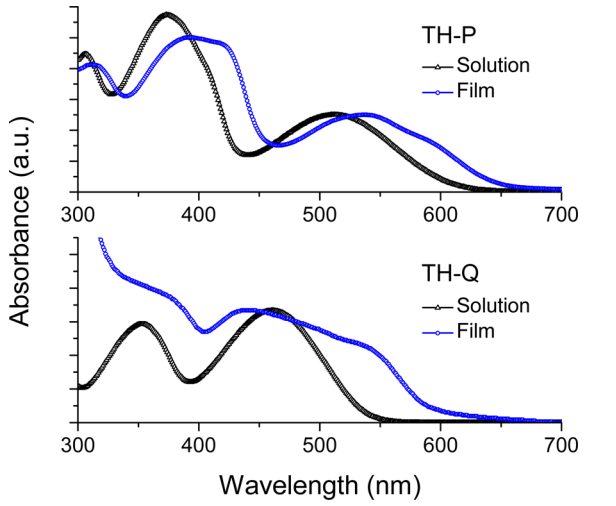

Figure 2. UV−vis spectra of **TH-P** and **TH-Q** in $CHCl_3$ and as cast films.

The examination of the cast films by field-emission scanning electron microscopy (FE-SEM) revealed that both films consist of fibers, proving the validity of the molecular design. However, a dramatic difference in the fiber morphology was observed. Shown in Figure 3, a network of endless, flexible fibers was formed from **TH-P** with significant fiber bundling. On the other hand, the fibers from **TH-Q** were needlelike, straighter, and more rigid.

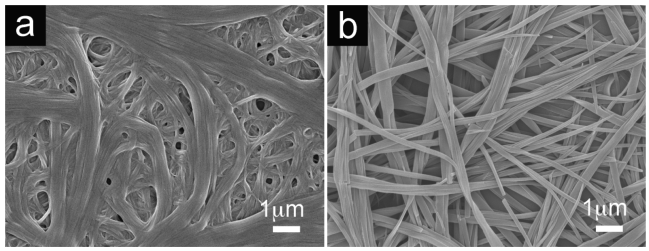

Figure 3. FE-SEM images of cast films: (a) **TH-P** and (b) **TH-Q**.

Both compounds had a sharp melting and crystallization transition measured by differential scanning calorimetry (DSC) (Figure S1). **TH-P** melted at a lower temperature (219.55 °C) than **TH-Q** (290.18 °C) due to the presence of flexible decyloxy side groups, and the same trend was observed for the crystallization temperature during the cooling scan. Both heats of transition (melting and crystallization) for **TH-Q** were almost 2 times higher than those for **TH-P**, indicating a higher degree of crystallinity for **TH-Q**. The decomposition temperature (T_d at 5% weight loss) for both compounds was quite

similar (356 °C for **TH-P** and 353 °C for **TH-Q**); however, a proper decomposition behavior of **TH-Q** was not measured due to significant sublimation during the thermogravimetric analysis (TGA) experiment (Figure S2).

Both cast films of **TH-P** and **TH-Q** were subjected to X-ray diffraction (XRD) measurements to investigate the molecular packing of the fibers. As shown in Figure 4, there are significant

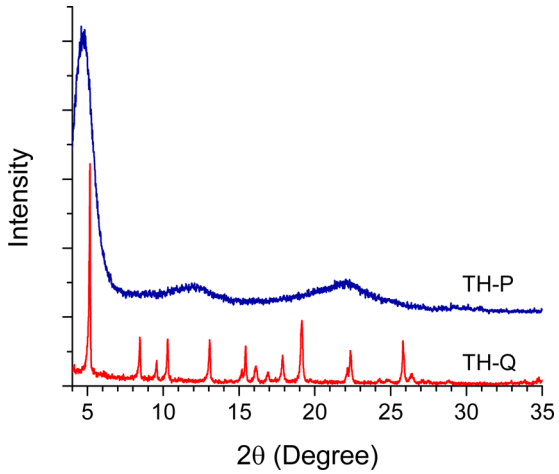

Figure 4. Powder XRD patterns of **TH-P** and **TH-Q** cast films.

differences in the diffraction patterns from the two samples. In general, **TH-Q** exhibited more defined peaks while **TH-P** showed a few broad peaks, which definitively indicates the higher crystallinity of **TH-Q**. In the case of **TH-Q**, the primary peak appeared at 2θ = 5.16° which corresponds to a *d*-spacing of 17.14 Å. The diffraction patterns also included second- and third-order peaks at $d/2$ (8.61 Å) and $d/3$ (5.74 Å), suggesting the formation of lamellar structures with a repeat distance of 17.14 Å. In addition, the appearance of diffraction peak at 2θ = 25.83° (*d*-spacing = 3.45 Å) may be assigned to $\pi-\pi$ stacking.[38,39] The observation of this $\pi-\pi$ stacking implies the existence of effective intermolecular π-orbital overlap, which is also supported by the red shifts in the solid-state absorption (Figure 2). Meanwhile, **TH-P** showed a strong diffraction peak only at 2θ = ca. 4.8° with a *d*-spacing of ca. 18.54 Å. The higher order diffraction peaks were not observed. The peak at 2θ = ca. 22° (*d*-spacing = ca. 4 Å) can be related to the $\pi-\pi$ stacking, often observed from ordered conjugated polymers.[25,26] The overall diffraction pattern of **TH-P** resembles those of polymeric materials, and indeed, the flexible fiber morphology from SEM images supports the XRD results. Note that **TH-Q** showed more significant red shift in the solid state relative to the solution absorption when compared with **TH-P**, which can be correlated to the shorter π-stacking distance. The primary *d*-spacings of both compounds are quite similar, and slightly shorter than the length of the molecules (20.54 Å from the thiophene on one end to the thiophene on the other end, estimated by a theoretical calculation at the B3LYP/6-31G* level). This suggests that molecules form layered structures in which the dithiophene−benzene−dithiopehene region of the molecule is aligned in a slightly tilted fashion.

The highest occupied molecular orbital (HOMO) and lowest unoccupied molecular orbital (LUMO) energies (E_{HOMO} and E_{LUMO}) estimated from cyclic voltammetry (CV) in solution were summarized in Figure S3. CV in the solid state was unsuccessful due to delamination of the films from the working electrode during the experiments. Both E_{HOMO} and E_{LUMO} were calculated from the onset of oxidation and reduction potentials, respectively, against ferrocene's (internal reference) oxidation potential of −4.8 eV with respect to vacuum. While E_{LUMO} of **TH-P** was −3.20 eV, 0.27 eV lower than that of **TH-Q** (−2.93 eV), the difference in E_{HOMO} was significantly less prominent. E_{HOMO} of **TH-P** (−5.06 eV) was only 0.06 eV higher than that of **TH-Q** (−5.12 eV). As a result, HOMO-LUMO energy gap (E_{gap}) of **TH-P** is smaller than that of **TH-Q**, which is consistent with the longer wavelength absorption of **TH-P** in solution (Figure 2). In addition, the trend in E_{HOMO} and E_{LUMO} was confirmed with theoretical evaluation. The calculation conducted on the optimized geometry at the B3LYP/6-31G* level showed that **TH-P** has higher electron affinity and a marginally lower oxidation potential than **TH-Q**.

The E_{gap} for these molecules are relatively low for such simple structures, and this interesting result was further investigated using frontier molecular orbital (FMO) diagrams. As shown in Figure 5, the HOMO and LUMO distribution

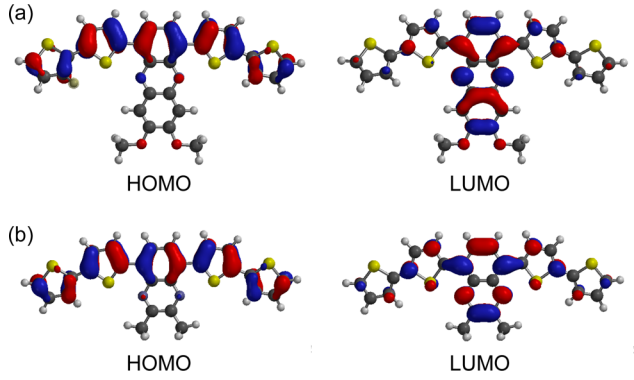

Figure 5. HOMO and LUMO orbital diagrams of (a) **TH-P** and (b) **TH-Q**. The orbital diagrams were generated by B3LYP/6-31G*.

resembles characteristic disjoint FMO structures[40] in which HOMO was distributed mainly on the electron-rich dithiophene−benzene−dithiophene while LUMO was located on the electron-deficient phenazine or quinoxaline cores, facilitating E_{gap} compression. As shown in Figure 5, the HOMO diagrams of the two molecules are essentially the same, which supports the similar E_{HOMO} of these two molecules estimated by CV (*vide supra*). However, more localization of LUMO on phenazine than quinoxaline was identified, resulting in lower E_{LUMO} of **TH-P** than that of **TH-Q**. This disjoint FMO distribution is very intriguing, and could further assist in molecular design to lower E_{gap} without increasing molecular size or complexity.

Considering E_{LUMO} of $PC_{61}BM$ (Figure S4), the two molecules can serve as donor materials to pair with $PC_{61}BM$ as the acceptor for BHJ OSCs. Therefore, OSC devices were fabricated in two configurations: (i) BHJ and (ii) planar bilayer heterojunction (PHJ)[41] using **TH-P** and **TH-Q** as donors and $PC_{61}BM$ as an acceptor. The general device structure was ITO/poly(3,4-ethylene-dioxythiophene):poly(styrenesulfonic acid) (PEDOT:PSS) (40 nm)/active layer/LiF/Al. The active layer, either BHJ or PHJ, was fabricated by spin-coating. For the BHJ of **TH-P**:$PC_{61}BM$, we attempted three different ratios between **TH-P** and $PC_{61}BM$; 1:05, 1:1, and 1:3 (w/w). The BHJ devices based on the ratio of 1:3 produced the highest power conversion efficiency (PCE), mainly due to the improved open-circuit voltage (V_{oc}). Current−voltage (J−V) character-

dx.doi.org/10.1021/am5027538 | ACS Appl. Mater. Interfaces 2014, 6, 15767−15773

istics are shown in Figures 6 and 7 and photovoltaic parameters from optimized devices are summarized in Table 1 (See Table

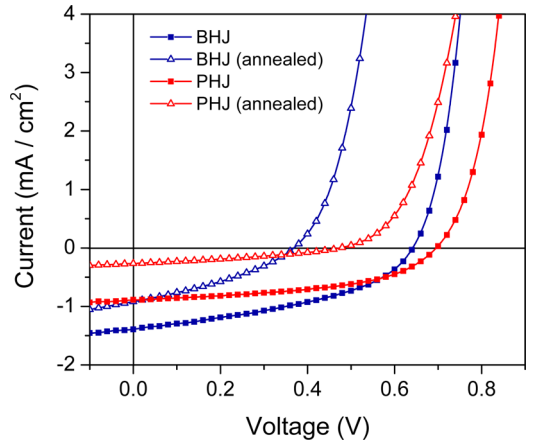

Figure 6. Characteristic J–V curves of BHJ and PHJ solar cells before and after thermal annealing using **TH-P** as a donor and $PC_{61}BM$ as an acceptor under 1 Sun condition (100 mW/cm^2).

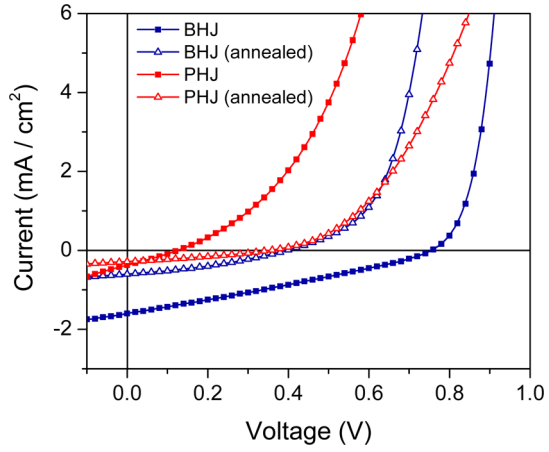

Figure 7. Characteristic J–V curves of BHJ and PHJ solar cells before and after thermal annealing using **TH-Q** as a donor and PCBM as an acceptor under 1 Sun condition (100 mW/cm^2).

S1 in ESI for photovoltaic performances of BHJ devices with different donor:$P_{61}BM$ compositions).

For the devices fabricated under the optimized conditions (i.e., 1:3 ratio and a film thickness of ca. 140 nm with dichloromethane (DCM) as the processing solvent), short-circuit current (J_{sc}), V_{oc}, fill factor (FF), and PCE obtained under AM1.5 (100 mW/cm^2) conditions were 1.54 mA/cm^2, 0.64 V, 38%, and 0.38%, respectively. Surprisingly, when the device was annealed at 150 °C for 30 min, which is well below the T_m, the PCE dropped to 0.11%. Both V_{oc} and J_{sc} decreased to 0.35 V and 0.96 mA/cm^2, respectively. This is opposite to trends with polymer-based BHJ where thermal annealing often improves PCE due to an increased J_{sc}.

Table 1. OSC Device Performance

	device type		V_{oc} (V)	J_{sc} (mA/cm^2)	FF (%)	PCE (%)
TH-P	BHJ[a]	pristine	0.64	1.54	38	0.38 ± 0.06
		annealed	0.35	0.96	34	0.11 ± 0.04
	PHJ	pristine	0.69	0.89	48	0.30 ± 0.05
		annealed	0.34	0.26	31	0.03 ± 0.02
TH-Q	BHJ[b]	pristine	0.74	1.63	30	0.36 ± 0.04
		annealed	0.40	0.62	35	0.09 ± 0.03
	PHJ	pristine	0.14	0.35	27	0.01 ± 0.00
		annealed	0.36	0.27	33	0.03 ± 0.01

[a]**TH-P**:$PC_{61}BM$ = 1:3 (w/w), [b]**TH-Q**:$PC_{61}BM$ = 1:1 (w/w). For more detailed fabrication conditions including PHJ devices, see the text and Supporting Information.

On the other hand, for PHJ devices with a structure of ITO/PEDOT:PSS (40 nm)/**TH-P**/$PC_{61}BM$/LiF/Al, the donor layer was fabricated by a spin-coating at a rate of 250 rpm using a **TH-P** solution in $CHCl_3$ (6 mg/mL). Subsequently, the $PC_{61}BM$ layer was prepared also by spin-coating at 1000 rpm with a DCM solution (8 mg/mL). The thickness of the combined two layers was 148 nm. The measured PCE under 1 Sun condition was 0.30%, slightly lower than that of BHJ. The decreased PCE was mainly due to the reduced J_{sc} (0.89 mA/cm^2) in the PHJ device when compared with that of the BHJ device. Note that V_{oc} of the two devices was very comparable. The effect of thermal annealing was even more dramatic. After annealing for 30 min at 150 °C, PCE dropped to 0.03%, an order of magnitude lower than that before annealing. As was the case of BHJ, the decrease in J_{sc} (3.4 times) was greater than the decrease in V_{oc} (2 times).

For **TH-Q**, the optimum donor material:$PC_{61}BM$ ratio was found to be 1:1 (w/w) among the ratios tested (1:0.5, 1:1, and 1:3), and the active layer was fabricated by spin-coating with a DCM solution (6 mg of donor material and 6 mg of $PC_{61}BM$ in 1 mL of DCM) at 1500 rpm. The thickness of the active layer was 61 nm. Under AM1.5 (100 mW/cm^2) condition, this BHJ device produced a V_{oc} of 0.74, a J_{sc} of 1.63 mA/cm^2, a FF of 30%, and a PCE of 0.36%. The V_{oc} was 0.1 V higher than that of BHJ from **TH-P**, which can be ascribed to the slightly lower E_{HOMO} of **TH-Q**. Again, thermal annealing gave negative effects, lowering PCE to 0.09%.

The fabrication conditions (concentration, solvent, and spin rate) for a PHJ based on **TH-Q** follows those for the **TH-P**-based PHJ. The thickness of the combined two layers was 61 nm. However, this device produced a negligible PCE, and the trend before and after thermal annealing did not follow those of other devices. This will be further discussed in the context of the morphological study (*vide infra*).

The external quantum efficiency (EQE) of BHJ devices (Figure 8) showed peaks of 22.4% at 415 nm for **TH-P** and 12.9% at 425 nm for **TH-Q**, which are consistent with the absorption maxima of the donor molecules.

To investigate the effect of thermal annealing, we conducted atomic force microscopy (AFM) studies on the devices before and after annealing. AFM images of BHJs made from **TH-P** and **TH-Q** are shown in Figure 9. To maintain the same condition as OSC characterization, we fabricated the donor (**TH-P** or **TH-Q**):$PC_{61}BM$ layer onto an ITO/PEDOT:PSS substrate. In the case of **TH-P**/$PC_{61}BM$, it is clear that the donor molecules form endless 1D fibers with a width of 300–400 nm upon spin-coating (Figure 9a). It is quite impressive that the molecules have a capability to assemble into homogeneous fibers in such a short time frame of solvent removal without having very strong intermolecular interactions such as hydrogen bonding. The $PC_{61}BM$ phase is well-dispersed in the three-dimensional fiber network, providing spontaneous phase separation and a large donor material/$PC_{61}BM$ surface area. The surface roughness of the BHJ was found to be ca. 90 nm, which is smaller than the fiber height due to the presence of $PC_{61}BM$.

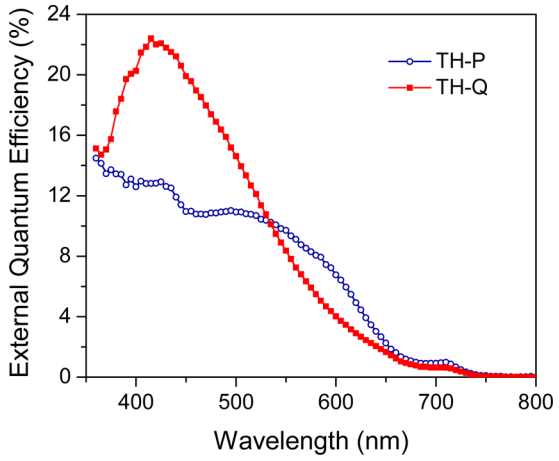

Figure 8. EQE spectra of BHJ devices based on **TH-P**/$PC_{61}BM$ and **TH-Q**/$PC_{61}BM$.

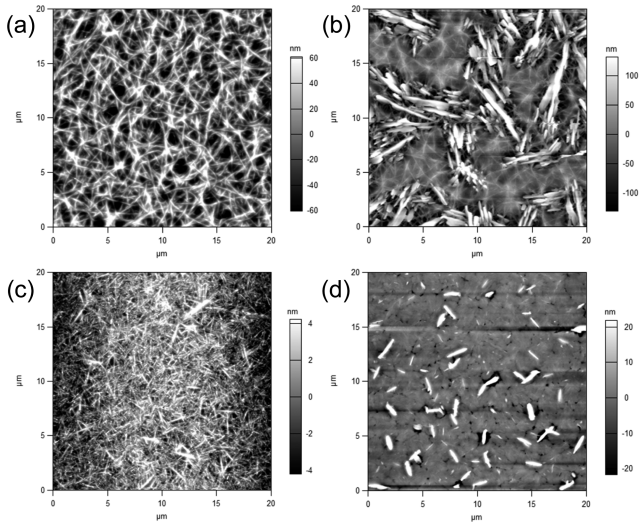

Figure 9. AFM images of BHJ from **TH-P**/$PC_{61}BM$ ((a) before and (b) after annealing) and **TH-Q**/$PC_{61}BM$ ((c) before and (d) after annealing).

A drastic change in morphology took place after thermal annealing. Most of the fiber network disappeared, and the domain size of the donor and acceptor phases increased significantly (Figure 9b). As a result of this morphological change, donor/$PC_{61}BM$ surface and charge-transport channels have been diminished, resulting in PCE reduction. The fibers from **TH-Q** showed a straight, short needlelike morphology in the BHJ, and they were quite well-dispersed (Figure 9c). The thickness had wide variations starting from ca. 150 nm due to bundling. Interestingly, **TH-Q**/$PC_{61}BM$ BHJ showed the surface roughness of ca. 8 nm. The annealing effect was very parallel to the **TH-P**/$PC_{61}BM$ BHJ. The original fiber morphology no longer existed, which accompanied larger domains of each component (Figure 9d). The results from the AFM study undoubtedly demonstrated that the fibrous morphology of the donor is beneficial for the OSC performance by providing built-in phase separation and charge-transport channels. Thermal annealing, essential for polymer-based BHJ, was detrimental to the current BHJ devices, presumably owing to low melt viscosity of the title compounds. Although the annealing temperature was lower than T_m of the donor molecules, their thermal mobility owing to the small molecular size allows for reorganization, leading to the disruption of the fiber networks.

Contrary to BHJs, PHJ based on the two donor molecules exhibited opposite device characteristics. While **TH-P**-based PHJ showed a PCE equivalent to its BHJ, **TH-Q**-based PHJ failed to perform. To investigate the surface morphology of the two PHJs, an AFM study was conducted on the first donor layer and the second $PC_{61}BM$ acceptor layer separately. In the case of the **TH-P** only layer (Figure S5a), the fiber morphology is reminiscent of those in the BHJ with a similar width and a somewhat larger height of 150−200 nm, and the substrate was well-covered with the fibers. The surface roughness and pores generated by the network of fibers serve as a natural source for a large D/A surface when the second $PC_{61}BM$ layer was deposited. In the case of the **TH-Q** only layer (Figure S6a), scattered large fibers were observed, and it seemed that **TH-Q** alone is not capable of producing homogeneous fibers with suitable surface coverage. The scattered fibers showed quite a heterogeneous size with 600−900 nm in width and 100−400 nm in height. Contrary to this result, the BHJ of **TH-Q**/$PC_{61}BM$ produced well-dispersed nice fibers, which was possible with the help of $PC_{61}BM$. It is clear that the device failure (PHJ) is due to the absence of a proper donor fiber network.

Finally, we measured the hole mobility of the donor materials in the absence and presence of $PC_{61}BM$ by space charge limited current (SCLC) method using a hole-only device configuration (ITO/PEDOT/active layer/MoO_3/Al). In the absence of $PC_{61}BM$, the hole mobilities of **TH-P** and **TH-Q** were 3.51×10^{-3} and 1.74×10^{-3} $cm^2\ V^{-1}\ s^{-1}$, respectively. In the presence of $PC_{61}BM$, both showed significantly lowered hole mobilities: 1.06×10^{-5} $cm^2\ V^{-1}\ s^{-1}$ for **TH-P** and 4.42×10^{-5} $cm^2\ V^{-1}\ s^{-1}$ for **TH-Q**. In this case, the ratios of donors:$PC_{61}BM$ were identical to those of BHJs, i.e., **TH-P**:$PC_{61}BM$ = 1:3 and **TH-Q**:$PC_{61}BM$ = 1:1. While relatively effective charge-transport pathways could form with the donor only, such pathways could be disrupted in the presence of $PC_{61}BM$, which lowers the hole mobility. The mobility of **TH-Q** is lower than that of **TH-P** in the absence of $PC_{61}BM$, and we ascribe this to the lack of fiber networks, as shown in the PHJ device (Figure S6a). In the presence of $PC_{61}BM$, nice fiber networks were formed, as revealed in the AFM image (Figure 9c), and the higher mobility of **TH-Q** in this case may be due to the higher crystallinity than that of **TH-P**. Interestingly, the mobility increased to 1.41×10^{-5} $cm^2\ V^{-1}\ s^{-1}$ for **TH-P** based BHJ device and 9.60×10^{-5} $cm^2\ V^{-1}\ s^{-1}$ for TH-Q based BHJ device after thermal annealing at 150 °C for 30 min. The thermal annealing can facilitate more ordered molecular organization, improving the hole mobility; however, undesired phase separation is also involved, affecting the PCE negatively.

The correlation of device performance to the morphology of the donor layers clearly demonstrates the necessity of continuous fibers. For small molecules, forming a high-quality film via spin-coating is difficult to obtain due to their tendency to crystallize and inability to stay on the substrate, overcoming the centrifugal force. However, as we showed in this study, the growth of a 3D network with continuous 1D fibers could be an effective approach to provide quality films via spin-coating. The final note we would like to make is on the fairly low J_{sc} values from the devices in this work. The spontaneous formation of fibers, though facilitating the intrafiber charge transport, could pose issues including reduced interfacial areas between these donor molecules with $PC_{61}BM$ for exciton to split, if the fiber

thickness is not properly controlled.[33] Finally, the relatively large band gaps of these small molecules limit the light absorption. All these factors, including low hole mobility, contribute to the fairly low J_{sc} we observed in our study. Further research to improve these aspects via molecular design is in progress.

CONCLUSIONS

In this paper, we have shown the significance of fibrillation of donor molecules in small-molecule-based solution-processed OSCs. The presented molecular donor systems are structurally simple yet powerful in producing 1D nanofibers via self-assembly, only with weak nonbonding interactions. The structural differences in the donor molecules influenced the fiber length and rigidity significantly, allowing for a comparative study on the effect of fiber morphology on the performance of OSCs. It was found that a 3D network of 1D fibers of the donor is valuable in generating built-in nanoscale phase separation from the $PC_{61}BM$ acceptor for a large D/A surface not only in BHJ but also in PHJ, as exemplified by **TH-P**. Post thermal treatment proved to give negative impacts on the PCE due to increased domain size, leading to decreased J_{sc}, which in turn emphasizes the necessity of fibrillation for efficient charge transport. Meanwhile, the system which assembles into short fibers has limitation in producing a continuous network by a fast spin-coating process (e.g., **TH-Q**). Finally, the current study provides a model 1D assembling donor platform from which further structural evolution can be made to improve OSC performance.

ASSOCIATED CONTENT

Supporting Information

Detailed synthetic procedures, DSC and TGA thermograms, cyclic voltammograms, graphical illustrations of E_{HOMO} and E_{LUMO}, AFM images of each layers for PHJ, BHJ device characteristics with different composition of donor:$PC_{61}BM$, and hole mobility measurement. This material is available free of charge via the Internet at http://pubs.acs.org.

AUTHOR INFORMATION

Corresponding Author

*E-mail: Dong-Chan.Lee@unlv.edu.

Author Contributions

The manuscript was written through contributions of all authors. All authors have given approval to the final version of the manuscript. All authors contributed equally.

Notes

The authors declare no competing financial interest.

ACKNOWLEDGMENTS

D.C.L. gratefully acknowledges financial support from NSF CAREER Award (DMR-0846479). L.Y. and W.Y. are supported by a NSF award (ECCS-1344745). We thank Prof. Kathleen Robins at the University of Nevada, Las Vegas, for providing molecular orbital diagrams of the title compounds.

REFERENCES

(1) Günes, S.; Neugebauer, H.; Sariciftci, N. S. Conjugated Polymer-Based Organic Solar Cells. *Chem. Rev.* **2007**, *107*, 1324−1338.
(2) Bundgaard, E.; Krebs, F. C. Low Band Gap Polymers for Organic Photovoltaics. *Sol. Energy Mater. Sol. Cells* **2007**, *91*, 954−985.
(3) Blom, P. W. M.; Mihailetchi, V. D.; Koster, L. J. A.; Markov, D. E. Device Physics of Polymer:Fullerene Bulk Heterojunction Solar Cells. *Adv. Mater.* **2007**, *19*, 1551−1566.
(4) Thompson, B. C.; Fréchet, J. M. J. Polymer-Fullerene Composite Solar Cells. *Angew. Chem., Int. Ed.* **2008**, *47*, 58−77.
(5) Kroon, R.; Lenes, M.; Hummelen, J. C.; Blom, P. W. M.; de Boer, B. Small Bandgap Polymers for Organic Solar Cells (Polymer Material Development in the Last 5 Years). *Polym. Rev.* **2008**, *48*, 531−582.
(6) Dennler, G.; Scharber, M. C.; Brabec, C. J. Polymer-Fullerene Bulk-Heterojunction Solar Cells. *Adv. Mater.* **2009**, *21*, 1323−1338.
(7) Cheng, Y.-J.; Yang, S.-H.; Hsu, C.-S. Synthesis of Conjugated Polymers for Organic Solar Cell Applications. *Chem. Rev.* **2009**, *109*, 5868−5923.
(8) Peet, J.; Heeger, A. J.; Bazan, G. C. Plastic Solar Cells: Self-Assembly of Bulk Heterojunction Nanomaterials by Spontaneous Phase Separation. *Acc. Chem. Res.* **2009**, *42*, 1700−1708.
(9) Beaujuge, P. M.; Fréchet, M. J. Molecular Design and Ordering Effects in π-Functional Materials for Transistor and Solar Cell Applications. *J. Am. Chem. Soc.* **2011**, *133*, 20009−20029.
(10) Zhou, H.; Yang, L.; You, W. Rational Design of High Performance Conjugated Polymers for Organic Solar Cells. *Macromolecules* **2012**, *45*, 607−632.
(11) He, Z.; Zhong, C.; Su, S.; Xu, M.; Wu, H.; Cao, Y. Enhanced Power-Conversion Efficiency in Polymer Solar Cells Using an Inverted Device Structure. *Nat. Photonics* **2012**, *6*, 591−595.
(12) Lu, L.; Yu, L. Understanding Low Bandgap Polymer PTB7 and Optimizing Polymer Solar Cells Based on It. *Adv. Mater.* **2014**, *26*, 4413−4430.
(13) Roncali, J. Molecular Bulk Heterojunctions: An Emerging Approach to Organic Solar Cells. *Acc. Chem. Res.* **2009**, *42*, 1719−1730.
(14) Walker, B.; Kim, C.; Nguyen, T.-Q. Small Molecule Solution-Processed Bulk Heterojunction Solar Cells. *Chem. Mater.* **2011**, *23*, 470−482.
(15) Sun, Y.; Welch, G. C.; Leong, W. L.; Takacs, C. J.; Bazan, G. C.; Heeger, A. J. Solution-Processed Small-Molecule Solar Cells with 6.7% Efficiency. *Nat. Mater.* **2012**, *11*, 44−48.
(16) Zhou, J.; Wan, Z.; Liu, Y.; Zuo, Y.; Li, Z.; He, G.; Long, G.; Ni, W.; Li, C.; Su, X.; Chen, Y. Small Molecule Based on Benzo[1,2:4,5-b′]dithiophene Unit for High-Performance Solution-Processed Organic Solar Cells. *J. Am. Chem. Soc.* **2012**, *134*, 16345−16351.
(17) Zhou, J.; Zuo, Y.; Wan, X.; Long, G.; Zhang, Q.; Ni, W.; Liu, Y.; Li, Z.; He, G.; Li, C.; Kan, B.; Li, M.; Chen, Y. Solution-Processed and High-Performance Organic Solar Cells Using Small Molecules with a Benzodithiophene Unit. *J. Am. Chem. Soc.* **2013**, *135*, 8484−8487.
(18) Kyaw, A. K. K.; Wang, D. H.; Gupta, V.; Leong, W. L.; Ke, L.; Bazan, G. C.; Heeger, A. J. Intensity Dependence of Current-Voltage Characteristics and Recombination in High-Efficiency Solution-Processed Small-Molecule Solar Cells. *ACS Nano* **2013**, *7*, 4569−4577.
(19) Kyaw, A. K. K.; Wang, D. H.; Gupta, V.; Zhang, J.; Chand, S.; Bazan, G. C.; Heeger, A. J. Efficient Solution-Processed Small-Molecule Solar Cells with Inverted Structure. *Adv. Mater.* **2013**, *25*, 2397−2402.
(20) Shin, W.; Yasuda, T.; Watanabe, G.; Yang, Y. S.; Adachi, C. Self-Organizing Mesomorphic Diketopyrrolopyrrole Derivatives for Efficent Solution-Processed Organic Solar Cells. *Chem. Mater.* **2013**, *25*, 2549−2556.
(21) Lim, N.; Cho, N.; Paek, S.; Kim, C.; Lee, J. K.; Ko, J. High-Performance Organic Solar Cells with Efficient Semiconducting Small Molecules Containing an Electron-Rich Benzodithiophene Derivatives. *Chem. Mater.* **2014**, *26*, 2283−2288.
(22) Berson, S.; De Bettignies, R.; Bailly, S.; Guillerez, S. Poly(3-hexylthiophene) Fibers for Photovoltaic Applications. *Adv. Funct. Mater.* **2007**, *17*, 1377−1384.
(23) Xin, H.; Kim, F. S.; Jenekhe, S. A. Highly Efficient Solar Cells Based on Poly(3-butylthiophene) Nanowires. *J. Am. Chem. Soc.* **2008**, *130*, 5424−5425.

(24) Wicklein, A.; Ghosh, S.; Sommer, M.; Würthner, F.; Thelakkat, M. Self-Assembly of Semiconductor Organogelator Nanowires for Photoinduced Charge Separation. *ACS Nano* **2009**, *3*, 1107−1114.
(25) Liu, F.; Gu, Y.; Jung, J. W.; Jo, W. H.; Russell, T. P. On the Morphology of Polymer-Based Photovoltaics. *J. Polym. Sci., Part B: Polym. Phys.* **2012**, *50*, 1018−1044.
(26) Liu, F.; Gu, Y.; Shen, X.; Ferdous, S.; Wang, H.-W.; Russell, T. P. Characterization of the Morphology of Solution-Processed Bulk Heterojunction Organic Photovoltaics. *Prog. Polym. Sci.* **2013**, *38*, 1990−2052.
(27) Li, C.; Chen, Y.; Zhao, Y.; Wang, H.; Zhang, W.; Li, Y.; Yang, X.; Ma, C.; Chen, L.; Zhu, X.; Tu, Y. Acceptor-Donor-Acceptor-Based Small Molecules with Varied Crystallinity: Processing Additive-Induced Nanofibril in Blend Film for Photovoltaic Applications. *Nanoscale* **2013**, *5*, 9536−9540.
(28) Wang, H.; Liu, F.; Bu, L.; Gao, J.; Wang, C.; Wei, W.; Russell, T. P. The Role of Additive in Diketopyrrolopyrrole-Based Small Molecular Bulk Heterojunction Solar Cells. *Adv. Mater.* **2013**, *25*, 6519−6525.
(29) Liu, F.; Wang, C.; Baral, J. K.; Zhang, L.; Watkins, J. J.; Briseno, A. L.; Russell, T. P. Relating Chemical Structure to Device Performance via Morphology Control in Diketopyrrolopyrrole-Based Low Band Gap Polymers. *J. Am. Chem. Soc.* **2013**, *135*, 19248−19259.
(30) Lam, K. H.; Foong, T. R. B.; Ooi, Z. E.; Zhang, J.; Grimsdale, A. C.; Lam, Y. M. Enhancing the Performance of Solution-Processed Bulk-Heterojunction Solar Cells Using Hydrogen-Bonding-Induced Self-Organization of Small Molecules. *ACS Appl. Mater. Interfaces* **2013**, *5*, 13265−13274.
(31) Li, W.; Hendriks, K. H.; Furlan, A.; Roelofs, W. S. C.; Wienk, M. M.; Janssen, R. A. J. Universal Correlation between Fibril Width and Quantum Efficiency in Diketopyrrolopyrrole-Based Polymer Solar Cells. *J. Am. Chem. Soc.* **2013**, *135*, 18942−18948.
(32) Harschneck, T.; Zhou, N.; Manley, E. F.; Lou, S. J.; Yu, X.; Butler, M. R.; Timalsina, A.; Turrisi, R.; Ratner, M. A.; Chen, L. X.; Chang, R. P. H.; Facchetti, A.; Marks, T. J. Substantial Photovoltaic Response and Morphology Tuning in Benzo[1,2-b:6,5-b′]-dithiophene(bBDT) Molecular Donors. *Chem. Commun.* **2014**, *50*, 4099−4101.
(33) Li, W.; Hendriks, K. H.; Furlan, A.; Roelofs, W. S. C.; Meskers, S. C. J.; Wienk, M. M.; Janssen, R. A. J. Effect of the Fibrillar Microstructure on the Efficiency of High Molecular Weight Diketopyrrolopyrrole-Based Polymer Solar Cells. *Adv. Mater.* **2014**, *26*, 1565−1570.
(34) Kimizuka, N.; Kawasaki, T.; Hirata, K.; Kunitake, T. Tube-like Nanostructures Composed of Networks of Complementary Hydrogen Bonds. *J. Am. Chem. Soc.* **1995**, *117*, 6360−6361.
(35) Würthner, F.; Thalacker, C.; Sautter, A. Hierarchical Organization of Functional Perylene Chromophores to Mesoscopic Superstructures by Hydrogen Bonding and π-π Interactions. *Adv. Mater.* **1999**, *11*, 754−758.
(36) Würthner, F.; Hanke, B.; Lysetska, M.; Lambright, G.; Harms, G. S. Gelation of a Highly Fluorescent Urea-Functionalized Perylene Bisimide Dye. *Org. Lett.* **2005**, *7*, 967−970.
(37) Kaiser, T. E.; Stepanenko, V.; Würthner, F. Fluorescent J-Aggregates of Core-Substituted Perylene Bisimides: Studies on Structure-Property Relationship, Nucleation-Elongation Mechanism, and Sergents-and Soldiers Principle. *J. Am. Chem. Soc.* **2009**, *131*, 6719−6732.
(38) Schmidt-Mende, L.; Fechtenkötter, A.; Müllen, K.; Moons, E.; Friend, R. H.; MacKenzie, J. D. Self-Organized Discotic Liquid Crystals for High-Efficiency Organic Photovoltaics. *Science* **2001**, *293*, 1119−1122.
(39) Briseno, A. L.; Mannsfeld, S. C. B.; Shamberger, P. J.; Ohuchi, F. S.; Bao, Z.; Jenekhe, S. A.; Xia, Y. Self-Assembly, Molecular Packing, and Electron Transport in n-Type Polymer Semiconductor Nanobelts. *Chem. Mater.* **2008**, *20*, 4712−4719.
(40) Zucchero, A. J.; McGrier, P. L.; Bunz, U. H. F. Cross-Conjugated Cruciform Fluorophores. *Acc. Chem. Res.* **2010**, *43*, 397−408.
(41) The PHJ device in this work does not represent a true bilayer configuration. Although the process was prompt, there may be certain level of dissolution of the donor fibers in $CHCl_3$ during the fabrication of the second $PC_{61}BM$ layer by spin-coating, which could cause a mixing of the donor and acceptor at the interface.